Vector Tracking Based on Factor Graph Optimization for GNSS NLOS Bias Estimation and Correction

Changhui Jiang, Yuwei Chen, Bing Xu, *Member, IEEE*, Jianxin Jia, Haibin Sun, Chen Chen, Zhiyong Duan, Yuming Bo, and Juha Hyyppä

***Abstract*—Position and location constitute critical context for Internet of Things (IoT) devices. Global navigation satellite systems (GNSSs) are the primary apparatus providing precise position and location information for IoT devices in outdoor environments. However, in dense urban areas, nonline-of-sight (NLOS) signals will induce large errors in GNSS pseudorange measurements due to the additional signal transmission paths. The vector tracking (VT) technique utilizing a Kalman filter (KF) to estimate navigation solutions has been investigated in NLOS detection, and its advantages have been demonstrated. However, the estimation of NLOS-induced bias has not been thoroughly investigated in the VT framework. In this article, we focus on the estimation and correction of NLOS-induced errors within the VT framework. First, graph optimization (GO) instead of a KF is incorporated with VT to optimize the estimation of navigation solutions. The NLOS-induced bias is then added to the VT state vector as the variable for real-time estimation. Compared with the KF-VT method, in GO-VT, the state transformation and the measurement model are regarded as constraints to optimize the state vector estimation. Hence, the GO-VT framework is more flexible than the KF approach in dealing with state vector changes. An iterative process is conducted to solve for the optimization results; a multiple-correlator scheme is employed in GO-VT to provide the initial values of the NLOS-induced bias. Three collected GPS L1 data sets (static and dynamic) are used to evaluate the proposed method. The statistical results support the conclusion that GO-VT with state augmentation achieves superior position estimation in urban areas.**

***Index Terms*—Factor graph optimization (FGO), global navigation satellite system (GNSS), Kalman filter (KF), nonline of sight (NLOS), vector tracking (VT).**

Manuscript received 25 September 2021; revised 6 December 2021; accepted 7 February 2022. Date of publication 11 February 2022; date of current version 24 August 2022. This work was supported in part by the Academy of Finland Projects "Ultrafast Data Production with Broadband Photodetectors for Active Hyperspectral Space Imaging," under Grant 336145, Forest-Human–Machine Interplay—Building Resilience, Redefining Value Networks and Enabling Meaningful Experiences (UNITE) under Grant 337656, and Strategic Research Council Project Competence-Based Growth Through Integrated Disruptive Technologies of 3-D Digitalization, Robotics, Geospatial Information and Image Processing/Computing—Point Cloud Ecosystem under Grant 314312; in part by the Chinese Academy of Science under Grant 181811KYSB20160113 and Grant XDA22030202; in part by the Beijing Municipal Science and Technology Commission under Grant Z181100001018036; in part by the Shanghai Science and Technology Foundations under Grant 18590712600; in part by Jihua Lab under Grant X190211TE190; in part by Huawei under Grant 9424877; and in part by the National Natural Science Foundation of China under Grant 42101445. *(Corresponding author: Yuwei Chen.)*

Changhui Jiang, Yuwei Chen, Jianxin Jia, Haibin Sun, and Juha Hyyppä are with the Department of Photogrammetry and Remote Sensing, Finnish Geospatial Research Institute, 02430 Masala, Finland (e-mail: changhui.jiang@nls.fi; yuwei.chen@nls.fi; jianxin.jia@nls.fi; haibin.sun@nls.fi; juha.hyyppä@nls.fi).

Bing Xu is with the Interdisciplinary Division of Aeronautical and Aviation Engineering, The Hong Kong Polytechnic University, Hong Kong (e-mail: pbing.xu@polyu.edu.hk).

Chen Chen is with the Department of Photogrammetry and Remote Sensing, Finnish Geospatial Research Institute, 02430 Masala, Finland, and also with the School of Automation, Nanjing University of Science and Technology, Nanjing 210094, China.

Zhiyong Duan is with the Department of Photogrammetry and Remote Sensing, Finnish Geospatial Research Institute, 02430 Masala, Finland, and also with the Department of Physical and Microelectronics and the Institute of Intelligent Sensing, Zhengzhou University, Zhengzhou 450001, China.

Yuming Bo is with the School of Automation, Nanjing University of Science and Technology, Nanjing 210094, China (e-mail: byming@njust.edu.cn).

Digital Object Identifier 10.1109/JIOT.2022.3150764

I. Introduction

With the significant advances in electronics and communications technologies in recent years, the usage of Internet of Things (IoT) devices and services has seen explosive growth [1]–[3]. IoT devices and techniques are helping to shape future society, industry, and human life. Position and location information is critical for massive-scale IoT devices and services. For outdoor applications, global navigation satellite systems (GNSSs) can generate precise position, velocity, and timing information [4], [5]. However, in urban areas, which are characterized by tall buildings and narrow streets, GNSS signals might be blocked or reflected, and the positioning errors are considerably exacerbated under these conditions [6]–[8]. A GNSS receiver generates measurements, i.e., pseudorange and pseudorange rates, by aligning the local signal replica and the incoming received signals. Position and velocity information is then obtained from the generated pseudorange and pseudorange rate measurements [6]–[8]. When the signals are all directly received by the antenna, the position and velocity are expected to be generated precisely. However, in urban areas, signal blockage will degrade the positioning accuracy; specifically, signal blockage will affect the geometric distribution of the signals. Signal reflection will contaminate the pseudorange measurements. Additional signal transmission paths will induce a time-varying bias in the pseudorange measurements [9]–[11].

In a conventional GNSS receiver, the signal tracking process is usually composed of carrier tracking [with a phase-locked loop (PLL) or a frequency-locked loop (FLL)] and

code tracking (with a delay-locked loop). Each channel works independently and accomplishes signal tracking individually [24]–[27]. This architecture, referred to as "scalar tracking," ignores the inherent relationship between the navigation solutions and signal tracking parameters [24]–[27]. Coops first proposed the vector tracking (VT) concept in the 1980s. At that time, GNSS signal tracking and navigation solution estimation were first integrated into a single functional block rather than separate blocks in the conventional GNSS receiver architecture [28]. Then, Spilker proposed a vector delay-locked loop (VDLL), which exploits the inherent relationship between position and code tracking [29]. Building on this background, VT has received wide attention and has been extensively investigated in the community [30]–[32]. Its benefits and robustness in challenging signal environments, e.g., environments with weak signals, highly dynamic conditions, interference, and signal outages, have been fully assessed and demonstrated [33]–[37]. In VT, the navigation solutions are fed back to calculate the signal tracking parameters. For code tracking, the position is utilized to calculate the code tracking parameters. When non-line-of-sight (NLOS) conditions occur, the position estimated with healthy satellites is utilized to calculate the code phase. The code phase difference between the NLOS-contaminated incoming signals and the local code replica reflects the NLOS reception state [38], [39]. Under NLOS conditions, the code phase difference containing the NLOS-induced bias should be estimated and compensated for.

II. Related Works

To guarantee GNSS positioning accuracy, NLOS signals must be detected and corrected [9]–[22]. Scientists and researchers in the community have given much attention to this problem, and various methods have been proposed and investigated for detecting NLOS conditions and correcting the resulting errors. According to a careful review of the literature, the proposed algorithms and methods can be divided into two different categories: 1) detection and 2) correction. NLOS signals usually have lower signal strength due to reflection, which could be a useful characteristic for classifying and identifying NLOS signals [9]–[11]. Apart from the signal power, various other features (elevation angle, delta pseudorange, etc.) extracted from the signal processing results can also be employed to classify NLOS signals with machine learning methods [support vector machines (SVMs); gradient boosting decision trees (GBDTs), etc.] [12]–[16]. Recently, deeper signal processing results known as correlator outputs have been employed in NLOS detection. NLOS and LOS signals have different correlator curves; NLOS signals have lower peaks in the correlator outputs, and there is a bias between the correlator peaks and the prompt correlator outputs [17], [18]. Correlator outputs are processed by deep learning neural networks [convolutional neural networks (CNNs)], and the features are automatically learned [17]. In addition, external information or environmental awareness, i.e., 3-D city models, sky-pointing fisheye cameras, and LiDAR, can be utilized to detect NLOS conditions [19]–[22]. With a 3-D city model or LiDAR data, the elevation angle of the boundary of the surrounding buildings can be extracted and compared to that of the satellites to detect NLOS conditions [19]–[22]. Additionally, with a sky-pointing fisheye camera, building boundaries can be extracted, and the satellites can then be projected onto the captured image for NLOS detection [19]–[22].

Once NLOS conditions have been detected, the two options are to exclude or correct the NLOS-contaminated measurements. Excluding such measurements from position estimation is an effective way to mitigate the negative influence of NLOS-induced errors on the position accuracy [19]–[22]. However, in dense urban areas, the available in-view satellites are limited due to signal blockage, and such mitigation will distort the geometric distribution of the in-view satellites. The resulting decrease in the number of in-view satellites and the distortion of the satellites' geometric distribution will degrade the GNSS position accuracy [22], [23]. Therefore, the better way is to correct the NLOS-contaminated measurements and include them in GNSS position estimation. With a 3-D model or LiDAR, the signal transmission paths can be traced, and the additional code phase delay can be extracted and applied to correct the NLOS-induced errors. However, unfortunately, the NLOS signal ray-tracing method is usually computationally intensive [22], [23]. Additionally, such external sensors or similar sources of aid are not always available. Therefore, a self-contained NLOS detection and correction method is preferable. Recently, an advanced GNSS signal processing method, VT, has been proposed and investigated for the detection of NLOS signals and the correction of the associated errors [22], [23].

VT-based NLOS detection and correction has recently been reported in [38] and [39]. Multiple correlators have been designed to extract the code bias, which is then employed to correct the NLOS-induced errors. In the conventional VT framework, a Kalman filter (KF) is usually utilized as the navigation filter to estimate the navigation solutions. The outputs of VDLL and VFLL discriminators are utilized to compose the measurement vector of the navigation filter. Specifically, the VDLL discriminator outputs are related to the positioning errors and local clock bias, and the VFLL discriminator outputs are related to the velocity errors and local clock drift [38], [39]. The navigation solutions estimated in the previous epoch are utilized to predict the signal tracking parameters, and in this manner, the state vectors are correlated in time [40]–[42]. Some variants of the KF have also been explored in VT to improve VT performance [40]–[42]. However, the KF ignores the time correlation between the state vectors. The uncertainty contained in the previous state vector might distort the recursive estimation of the current state vector in the KF. In our recent work, we investigated the feasibility of using an optimization method as the navigation estimator in VT [43]. However, only a limited smoothing window size was utilized, and NLOS-induced bias was not considered. In this article, we first construct a factor graph optimization (FGO)-VT procedure using the well-known opensource graph optimization library GTSAM [44]. The NLOS-induced bias is added to the state vector as an unknown variable for real-time estimation. Multiple correlators

are utilized to provide initial values for the NLOS-induced bias state. The FGO method has the advantage of "plug-and-play" characteristics for flexibly dealing with state or measurement vector changes. The contributions of this work are summarized as follows.

1) An FGO-VT technique is proposed, in which the KF is replaced with the FGO method as the navigation filter for VT. Model factors and clock factors are defined to construct the graph. As more state vectors are estimated and optimized via FGO, smoother results are expected due to fuller utilization of the past measurements and state vector propagation relationships. Additionally, FGO-VT is more flexible in dealing with the state or measurement vector changes.
2) The NLOS-induced bias is added to the state vector for real-time estimation, and multiple correlators are employed to extract the initial values of the NLOS-induced bias. The FGO method is then used to optimize the estimation through an iterative process to realize better correction of NLOS-induced errors.

The following section describes the KF-VT technique, including the VT navigation filters, state equation, and measurement equation, as well as the LOS/NLOS signal model and the new navigation filter model under NLOS conditions. Then, the experimental section follows, which describes how three GPS L1 IF data sets were employed to assess the proposed method. Detailed results and in-depth analysis are presented for thorough assessment. Finally, we discuss the results and conclude this article.

III. Kalman-Filter-Based Vector Tracking

In this section, we present the VT navigation filter under LOS conditions; then, the LOS and NLOS signal models are given. Finally, the VT navigation filter considering the NLOS-induced bias as a state variable is introduced.

A. VT Navigation Filter Model Under LOS Conditions

As mentioned in Section I, VT utilizes a navigation filter to estimate navigation solutions using correlator output measurements. The VT module employed in this work is composed of a VDLL and a vector frequency-locked loop (VFLL) [38], [39]. Specifically, the VDLL and VFLL discriminator outputs are utilized as the measurements for the VT navigation filter. In a typical VT navigation filter, the state vector $\delta\mathbf{x}$ comprises positioning errors, velocity errors, and clock-related errors. $\delta\mathbf{x}$ is usually defined as follows [38], [39]:

$$\Delta\mathbf{x} = \left[\Delta\mathbf{pos},\, \Delta\mathbf{vel},\, \Delta t_b,\, \Delta t_d\right]^{\mathrm{T}} \tag{1}$$

where the vector $\delta\mathbf{pos}$ denotes the three-axis VT positioning errors in the earth-centered earth-fixed (ECEF) coordinate system, the vector $\delta\mathbf{vel}$ denotes the VT velocity errors in the ECEF coordinate system, δt_b denotes the user clock bias error in units of meters, and δt_d denotes the user clock drift error in units of meters per second.

The VT navigation filter system propagation equation is

$$\Delta\mathbf{x}_{k+1} = \mathbf{F}_{k,k+1}\cdot\Delta\mathbf{x}_k + \mu_k \tag{2}$$

where μ_k denotes the process noise vector of the state model, which is assumed to be subject to a Gaussian distribution with zero mean; the covariance matrix of the state model process noise vector μ_k is $\mathbf{Q}_k$; and $\mathbf{F}_{k,k+1}$ denotes the state transformation matrix between the kth and $(k+1)$th epochs. Specifically, its equation is

$$\mathbf{F}_{k,k+1} = \begin{bmatrix} \mathbf{I}_{3\times3} & \mathbf{I}_{3\times3}\cdot T_0 & \mathbf{0}_{3\times2} \\ \mathbf{0}_{3\times3} & \mathbf{I}_{3\times3} & \mathbf{0}_{3\times2} \\ \mathbf{0}_{2\times3} & \mathbf{0}_{2\times3} & \begin{bmatrix} 1 & T_0 \\ 0 & 1 \end{bmatrix} \end{bmatrix} \tag{3}$$

where the matrix $\mathbf{I}_{3\times3}$ is the identity matrix and the variable T_0 is the update interval of the VT navigation filter, which usually takes a value of 1 ms.

For VT, the VFLL is utilized for carrier tracking, and the VDLL performs code tracking. The relationship between the velocity error $\delta\mathbf{vel}_{k+1}^{\mathrm{T}}$ and the pseudorange rate error measurements (VFLL carrier discriminator outputs) $\delta\mathbf{z}_{k+1}^{prr}$ can be modeled as follows [38], [39]:

$$\mathbf{z}_{k+1}^{prr} = \mathbf{H}_{k+1}^{prr}\cdot\Delta\mathbf{vel}_{k+1}^{\mathrm{T}} + \begin{bmatrix} 1 & 1 & \cdots & 1 \end{bmatrix}_{1\times N}^{\mathrm{T}} \times\ \Delta t_{d,k+1} + \boldsymbol{\eta}_k^{prr} \tag{4}$$

with

$$\mathbf{H}_{k+1}^{prr} = \begin{bmatrix} -\mathrm{LOS}_x^{(1)} & -\mathrm{LOS}_y^{(1)} & -\mathrm{LOS}_z^{(1)} \\ -\mathrm{LOS}_x^{(2)} & -\mathrm{LOS}_y^{(2)} & -\mathrm{LOS}_z^{(2)} \\ \vdots & \vdots & \vdots \\ -\mathrm{LOS}_x^{(N)} & -\mathrm{LOS}_y^{(N)} & -\mathrm{LOS}_z^{(N)} \end{bmatrix}_{N\times3} \tag{5}$$

$$\left[-\mathrm{LOS}_x^{(i)} - \mathrm{LOS}_y^{(i)} - \mathrm{LOS}_z^{(i)}\right] = \left(\mathbf{pos}^{(i)} - \mathbf{pos}_u\right) \Big/ \left\|\mathbf{pos}^{(i)} - \mathbf{pos}_u\right\| \tag{6}$$

where $\mathbf{pos}^{(i)}$ and $\mathbf{pos}_u$ denote the position vectors of the ith satellite and the user receiver, respectively, and $\boldsymbol{\eta}_k^{prr}$ represents the measurement noise vector, which has dimensions of $N\times1$.

The relationship between the code errors (discriminator outputs) $\delta\mathbf{z}_{k+1}^{\mathrm{pr}}$ and the positioning error $\delta\mathbf{pos}$ is modeled as follows:

$$\mathbf{z}_{k+1}^{\mathrm{pr}} = \mathbf{H}_{k+1}^{\mathrm{pr}}\cdot\Delta\mathbf{pos}_{k+1}^{\mathrm{T}} + \begin{bmatrix} 1 & 1 & \cdots & 1 \end{bmatrix}_{1\times N}^{\mathrm{T}} \times\ \Delta t_{b,k+1} + \boldsymbol{\eta}_{k+1}^{\mathrm{pr}} \tag{7}$$

where $\mathbf{H}_{k+1}^{\mathrm{pr}}$ denotes the pseudorange measurement observation matrix, which is identical to the pseudorange rate measurement observation matrix $\mathbf{H}_{k+1}^{prr}$, and $\boldsymbol{\eta}_{k+1}^{\mathrm{pr}}$ denotes the measurement noise vector. The VT navigation filter model is written as

$$\Delta\mathbf{z}_{k+1} = \begin{bmatrix} \Delta\mathbf{z}_{k+1}^{\mathrm{pr}} \\ \Delta\mathbf{z}_{k+1}^{prr} \end{bmatrix} = \mathbf{H}_{k+1}\cdot\Delta\mathbf{x}_{k+1} + \begin{bmatrix} \boldsymbol{\eta}_{k+1}^{prr} \\ \boldsymbol{\eta}_{k+1}^{prr} \end{bmatrix} \tag{8}$$

with

$$\mathbf{H}_{k+1} = \begin{bmatrix} \mathbf{H}_{k+1}^{\mathrm{pr}} & \mathbf{0}_{N\times3} & \mathbf{A} \\ \mathbf{0}_{N\times3} & \mathbf{H}_{k+1}^{prr} & \mathbf{B} \end{bmatrix} \tag{9}$$

$$\mathbf{A} = \begin{bmatrix} 1 & 0 \\ 1 & 0 \\ \vdots & \vdots \\ 1 & 0 \end{bmatrix}_{N\times2} \tag{10}$$

$$\mathbf{B} = \begin{bmatrix} 0 & 1 \\ 0 & 1 \\ \vdots & \vdots \\ 0 & 1 \end{bmatrix}_{N\times 2}. \tag{11}$$

With the state and measurement models illustrated in (1)–(11), a KF is usually employed to estimate the state vector. The KF works recursively in a two-step process. In the first step, the KF predicts the state vector and the state estimation error covariance matrix. The equations are

$$\Delta\mathbf{x}_{k+1}^{-} = \mathbf{F}_{k,k+1} \cdot \Delta\mathbf{x}_k \tag{12}$$

$$\mathbf{P}_{k+1}^{-} = \mathbf{F}_{k,k+1} \cdot \mathbf{P}_k \left(\mathbf{F}_{k,k+1}\right)^{\mathrm{T}} + \mathbf{Q}_k \tag{13}$$

where $\delta\mathbf{x}_{k+1}^{-}$ is the predicted state vector; $\mathbf{P}_k$ represents the state estimation error covariance matrix; $\mathbf{P}_{k+1}^{-}$ is the predicted state estimation error covariance matrix; $\mathbf{Q}_k$ denotes the state process noise covariance matrix, $\mathbf{Q}_k = E(\mu_k \mu_k^{\mathrm{T}})$; and $E(\cdot)$ denotes the function for calculating the expectation.

Once the state vector and state estimation error covariance matrix have been predicted, the second step is to update the state vector and state estimation error covariance matrix in a weighted manner. The equations for the update procedure are

$$\Delta\mathbf{x}_{k+1} = \Delta\mathbf{x}_{k+1}^{-} + \mathbf{K}_{k+1}\left(\mathbf{z}_{k+1} - \mathbf{H}_{k+1}\Delta\mathbf{x}_{k+1}^{-}\right) \tag{14}$$

$$\mathbf{K}_{k+1} = \mathbf{P}_{k+1}^{-}(\mathbf{H}_{k+1})^{T}\left[\mathbf{H}_{k+1}\mathbf{P}_{k+1}^{-}(\mathbf{H}_{k+1})^{\mathrm{T}} + \mathbf{R}_{k+1}\right]^{-1} \tag{15}$$

$$\mathbf{P}_{k+1} = (\mathbf{I} - \mathbf{K}_{k+1}\mathbf{H}_{k+1})\mathbf{P}_{k+1}^{-} \tag{16}$$

where $\mathbf{K}_{k+1}$ denotes a Kalman gain matrix with dimensions of $8 \times N$, $\mathbf{I}$ denotes the identity matrix, and $\mathbf{R}_{k+1}$ represents the covariance matrix of the measurement noise, which is calculated as $\mathbf{R}_k = E(\boldsymbol{\eta}_k \boldsymbol{\eta}_k^{\mathrm{T}})$ with $\boldsymbol{\eta}_k = [\eta_{k+1}^{prr} \quad \eta_{k+1}^{prr}]^T$.

B. LOS/NLOS Signal Model

In a GNSS, satellites broadcast signals to the Earth, and a user equipped with an antenna receives the signals. After sampling, amplification, and downconversion by the user's receiver, an intermediate-frequency (IF) data set is obtained. According to a careful review of the literature, the IF signal model can be written as follows [15], [38]:

$$y_{\mathrm{LOS}}(j \cdot T_s) = A \cdot C(j \cdot T_s - \tau_0)\cos((\omega_{IF} + \omega_d) \cdot j \cdot T_s + \varphi_0) + w_{\mathrm{LOS}}(j \cdot T_s) \tag{17}$$

$$y_{\mathrm{NLOS}}(j \cdot T_s) = \alpha_{\mathrm{NLOS}} \cdot A \cdot C(j \cdot T_s - \tau_0 - \tau_{\mathrm{NLOS}}) \times \cos\{(\omega_{IF} + \omega_d) \cdot j \cdot T_s + \varphi_0 + \Delta\varphi_{\mathrm{NLOS}} + \Delta\omega_{\mathrm{NLOS}} \cdot j \cdot T_s\} + w_{\mathrm{NLOS}}(j \cdot T_s) \tag{18}$$

where y_{LOS} and y_{NLOS} denote the values of the sampled signals, j represents the index of the sampled signals, T_s denotes the sampling time duration, A represents the signal amplitude, $C(\cdot)$ is the pseudorandom noise (PRN) code modulated in the navigation signals, τ_0 is the initial code phase of the signals, τ_{NLOS} is the additional code phase induced by the occurrence of NLOS signal reflection, ω_{IF} denotes the IF signal frequency, ω_d denotes the Doppler shift contained in the received signals, φ_0 denotes the initialized carrier phase, $\Delta\varphi_{\mathrm{NLOS}}$ denotes the additional carrier phase induced by the occurrence of NLOS signal reflection, the variable α_{NLOS} represents the NLOS reflection coefficient, and $w_{\mathrm{LOS}}(i \cdot T_s)$ and $w_{\mathrm{NLOS}}(i \cdot T_s)$ denote the noise contained in the LOS and NLOS signals, respectively, which is usually assumed to be subject to a Gaussian distribution with zero mean [15].

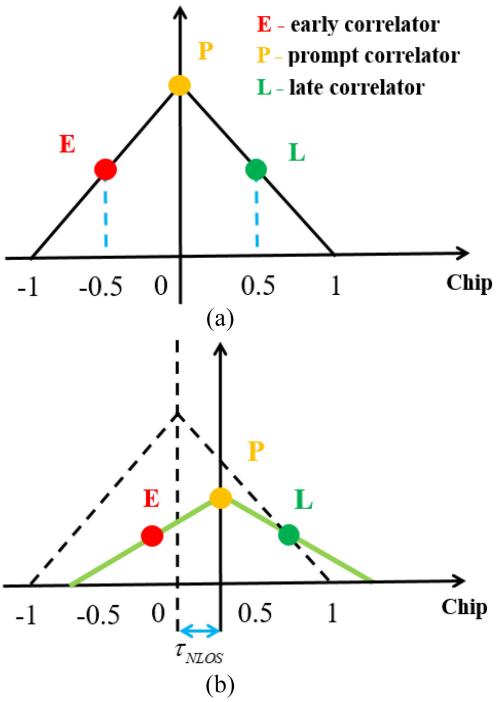

Fig. 1. Correlator outputs for GNSS NLOS/LOS signals [38]. (a) Correlator outputs for a LOS signal. (b) Correlator outputs for an NLOS signal.

The core of GNSS signal tracking is to align the local replica with the received signals [7]. In this way, the signal parameters (code phase and Doppler shift) are extracted. In VT, the code phase is related to the positioning errors, and the Doppler shift is related to the velocity errors. The code discriminator and carrier-frequency discriminator outputs are employed as the measurements in the VT navigation filter to estimate the navigation solutions [38], [39]. Then, the estimated navigation solutions are utilized to calculate the signal parameters of the local signal replica. Generally, the carrier and code discriminator outputs are calculated using the correlation results between the local signal replica and the received signals. Usually, three correlators, namely, an early correlator (E), a prompt (P) correlator, and a late correlator (L), with a code spacing of 0.5 are set up to correlate with the received incoming signals [38], [39]. Fig. 1 presents the correlators' outputs for LOS and NLOS signals. Under LOS conditions, the peak of the correlator output should be consistent with the prompt correlator output [38], [39]. Under NLOS conditions, due to the additional signal reflection, there will be a positive code phase bias. Additionally, the magnitude of the correlator outputs will be lower than in the case of LOS signals. When NLOS conditions occur, a bias will be added to the code phase measurements listed in (7). After NLOS detection, the key is to estimate this bias and correct it.

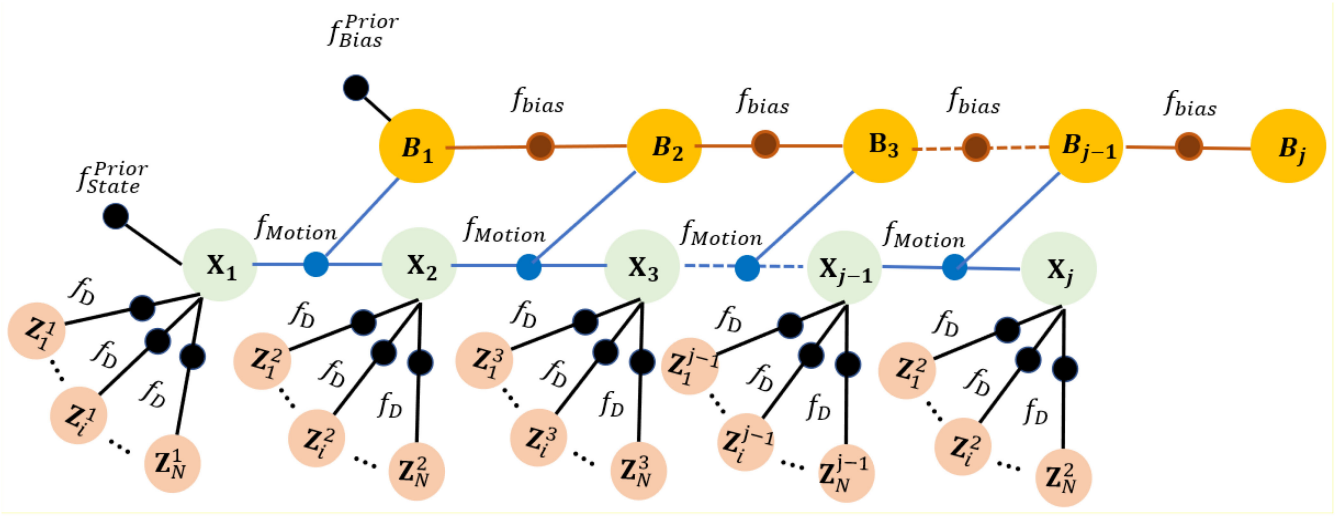

Fig. 2. Factor graph.

C. VT Navigation Filter Model Under NLOS Conditions

As mentioned above, the additional code bias induced by NLOS reception will cause the quality of the navigation solutions to degrade. Therefore, before the code measurements are passed to the navigation filter for navigation solution estimation, the NLOS-induced code bias should be estimated and corrected. Instead of directly excluding NLOS measurements, this article proposes adding the NLOS-induced code bias to the state vector for real-time estimation. Under NLOS conditions, the pseudorange measurement model is written as

$$\mathbf{z}_{k+1}^{\mathrm{pr}} = \mathbf{H}_{k+1}^{\mathrm{pr}} \cdot \Delta \mathbf{p}_{k+1}^{\mathrm{T}} + c \cdot \Delta t_{b,k+1} + \mathbf{b}^{\mathrm{NLOS}} + \boldsymbol{\eta}_{k+1}^{\mathrm{pr}} \quad (19)$$

where $\mathbf{b}^{\mathrm{NLOS}}$ denotes the NLOS-induced pseudorange measurement error. After the NLOS-induced bias is added to the state vector, the new state vector is constructed as

$$\mathbf{x}^{\mathrm{NLOS}} = \left[\Delta \mathbf{pos}, \Delta \mathbf{vel}, \Delta t_b, \Delta t_d, \mathbf{b}^{\mathrm{NLOS}}\right]^{\mathrm{T}}. \quad (20)$$

Additionally, the state and measurement models are rewritten as

$$\Delta \mathbf{x}_{k+1}^{\mathrm{NLOS}} = \mathbf{F}_{k,k+1}^{\mathrm{NLOS}} \Delta \mathbf{x}_{k}^{\mathrm{NLOS}} + \mu_{k+1}^{\mathrm{NLOS}} \quad (21)$$

$$\mathbf{z}_{k+1}^{\mathrm{NLOS}} = \mathbf{H}_{k+1}^{\mathrm{NLOS}} \cdot \Delta \mathbf{x}_{k+1}^{\mathrm{NLOS}} + \boldsymbol{\eta}_{k+1}^{\mathrm{NLOS}} \quad (22)$$

where

$$\mathbf{F}_{k,k+1}^{\mathrm{NLOS}} = \begin{bmatrix} \mathbf{F}_{k,k+1} & \mathbf{0} \\ \mathbf{0} & \mathbf{I} \end{bmatrix} \quad (23)$$

$$\mathbf{H}_{k+1}^{\mathrm{NLOS}} = \begin{bmatrix} \mathbf{H}_{k+1}^{\mathrm{pr}} & \mathbf{0}_{N\times 3} & \mathbf{A} & \mathbf{C}_{N\times 1} \\ \mathbf{0}_{N\times 3} & \mathbf{H}_{k+1}^{prr} & \mathbf{B} & \mathbf{0}_{N\times 1} \end{bmatrix}. \quad (24)$$

$\mathbf{F}_{k,k+1}$ is the state transformation matrix given in (3), and $\mathbf{C}_{N\times 1}$ is a matrix with values of 1 and 0 for NLOS and LOS conditions, respectively. The state vectors can be estimated using the KF given in (12)–(16).

IV. Factor Graph Optimization Method

It can be observed that the state and measurement models are represented and modeled in terms of matrices, and they are connected through the state transformation and observation matrix. The optimal state estimate is solved for by minimizing the state transformation and measurement errors in consecutive epochs. In contrast, in FGO, the connection between the states and measurements is represented by a graphic model; Fig. 2 presents the structure of the factor graph for VT considering NLOS bias. Normally, the optimal state estimation problem is solved for given measurements, and the factorization function determined from the factor graph is given as follows [7]:

$$f(\boldsymbol{\chi}) = \prod_i f_i(\boldsymbol{\chi}_i) \quad (25)$$

where $\boldsymbol{\chi}_i$ denotes the state nodes and edges are utilized to connect the nodes with the factors f_i.

In FGO, the optimal state estimate $\hat{\boldsymbol{\chi}}$ is solved for by minimizing the entire cost function, and the model is written as

$$\hat{\boldsymbol{\chi}} = \arg\min_{\boldsymbol{\chi}} \left(\prod_i f_i(\boldsymbol{\chi}_i) \right). \quad (26)$$

Furthermore, the optimization problem can be converted into a maximum *a posteriori* (MAP) problem. Suppose that the state process noise and the measurement noise are subject to Gaussian distributions with covariance matrices $\boldsymbol{\Sigma}_k$ and $\boldsymbol{\Lambda}_k$. The MAP problem is given by

$$\hat{\mathbf{X}} = \arg\max \prod P(\mathbf{Z}_i|\mathbf{X}_i) \prod P(\mathbf{X}_i|\mathbf{X}_{i-1}, \mathbf{u}_i) \quad (27)$$

$$P(\mathbf{Z}_i|\mathbf{X}_i) \propto \exp\left(-\frac{1}{2} \left\| h_i(\mathbf{X}_{i-1}, \mathbf{u}_i) - \mathbf{X}_i \right\|_{\boldsymbol{\Sigma}_i}^2 \right) \quad (28)$$

$$P(\mathbf{Z}_i|\mathbf{X}_i) \propto \exp\left(-\frac{1}{2} \| h_i(\mathbf{X}_{i-1}) - \mathbf{X}_i \|_{\boldsymbol{\Lambda}_i}^2 \right). \quad (29)$$

Ultimately, the MAP problem is converted into a nonlinear least squares problem, and the optimal state estimate is written as

$$\hat{\mathbf{X}} = \arg\min \left(\sum_{i=1}^{K} \left\| f_i(\mathbf{X}_{i-1}, \mathbf{u}_i) - \mathbf{X}_i \right\|_{\boldsymbol{\Sigma}_i}^2 + \sum_{i=1}^{K} \| h_i(\mathbf{X}_{i-1}) - \mathbf{X}_i \|_{\boldsymbol{\Lambda}_i}^2 \right) \quad (30)$$

where $\|\cdot\|$ is the Mahalanobis norm, $\mathbf{Z}_i$ denotes the measurement vector, $\mathbf{u}_i$ denotes the control input, and $\hat{\mathbf{X}}$ denotes the optimal states.

A. Factors and Error Functions

In the factor graph structure presented in Fig. 2, there are three factors: 1) a motion factor; 2) a discriminator factor; and 3) the NLOS bias factor. Let the factor graph for VT considering NLOS bias be denoted by $\mathbf{X} = (\mathbf{x}, \mathbf{B})$; the details and related equations are given as follows.

1) *Motion Factor:* Two consecutive states are connected through the model as expressed below

$$\mathbf{x}_{j+1} = h_{\text{motion}}(\mathbf{x}_j) + N\left(0, \boldsymbol{\Sigma}_j^{\text{motion}}\right) \tag{31}$$

where $h_{\text{motion}}(\cdot)$ denotes a function that is similar to (2). Therefore, the error function of the motion factor is expressed as

$$\left\|\mathbf{e}_{j+1}^{\text{motion}}\right\|^2_{\boldsymbol{\Sigma}_{j+1}^{\text{motion}}} = \left\|\mathbf{x}_{j+1} - h_{\text{motion}}(\mathbf{x}_j)\right\|^2_{\boldsymbol{\Sigma}_{j+1}^{\text{motion}}}. \tag{32}$$

2) *VT Discriminator Factor:* Similar to the measurement model given for the KF method, the discriminator outputs are utilized as the measurements considered in the state estimation process. The relationship between the states and measurements is expressed as

$$\mathbf{Z}_{j+1} = h_D(\mathbf{x}_{j+1}, \mathbf{B}_{j+1}) + N\left(0, \boldsymbol{\Sigma}_{j+1}^{D}\right). \tag{33}$$

Accordingly, the error function is written as

$$\left\|\mathbf{e}_{j+1}^{D}\right\|^2_{\boldsymbol{\Sigma}_{j+1}^{D}} = \left\|\mathbf{Z}_{j+1} - h_D(\mathbf{x}_{j+1}, \mathbf{B}_{j+1})\right\|^2_{\boldsymbol{\Sigma}_{j+1}^{D}}. \tag{34}$$

3) *NLOS Bias Factor:* The NLOS bias between two consecutive epochs is modeled as

$$\mathbf{B}_{j+1} = h_B(\mathbf{B}_j) + N\left(0, \boldsymbol{\Sigma}_j^{B}\right). \tag{35}$$

Accordingly, the error function is expressed as

$$\left\|\mathbf{e}_{j+1}^{B}\right\|^2_{\boldsymbol{\Sigma}_{j+1}^{B}} = \left\|\mathbf{B}_{j+1} - h_B(\mathbf{B}_j)\right\|^2_{\boldsymbol{\Sigma}_{j+1}^{B}}. \tag{36}$$

For FGO-VT considering NLOS-induced bias, we use the above three factors to formulate the optimal estimation of the state vectors as follows:

$$\mathbf{X}^* = \arg\min \left(\left\|\mathbf{e}_{j+1}^{\text{motion}}\right\|^2_{\boldsymbol{\Sigma}_{j+1}^{\text{motion}}} + \left\|\mathbf{e}_{j+1}^{D}\right\|^2_{\boldsymbol{\Sigma}_{j+1}^{D}} + \left\|\mathbf{e}_{j+1}^{B}\right\|^2_{\boldsymbol{\Sigma}_{j+1}^{B}}\right) \tag{37}$$

where $\mathbf{X}^*$ denotes the set of state vectors.

B. Levenberg–Marquardt Method

In this article, we utilize the opensource library GTSAM [41], [42] to implement FGO, and we define the above three factors with this library. Here, we select the Levenberg–Marquardt (LM) method to solve for the optimal states using the error function given in (37). To illustrate the LM method, the error function is written in a general form

$$\mathbf{F}(\mathbf{Y}) = \sum \mathbf{cost}_i \cdot \boldsymbol{\Omega} \cdot (\mathbf{cost}_i)^T \tag{38}$$

where $\mathbf{Y}$ denotes the vectors, $\boldsymbol{\Omega}$ represents the inverse of the covariance matrix, and $\mathbf{cost}_i$ represents the cost function. Generally, there are three essential steps in the LM method [41], [42].

First, the first-order Taylor expansion of the cost function $\mathbf{F}(\mathbf{Y})$ is calculated at $\tilde{\mathbf{Y}}$, yielding

$$\mathbf{cost}_i\left(\tilde{\mathbf{Y}} + \Delta\mathbf{Y}\right) \cong \mathbf{cost}_i + \mathbf{Jac}_i \cdot \Delta\mathbf{Y} \tag{39}$$

$$\begin{aligned}\mathbf{F}_i\left(\tilde{\mathbf{Y}} + \Delta\mathbf{Y}\right) &= \mathbf{cost}_i\left(\tilde{\mathbf{Y}} + \Delta\mathbf{Y}\right) \cdot \boldsymbol{\Omega} \cdot \left(\mathbf{cost}_i\left(\tilde{\mathbf{Y}} + \Delta\mathbf{Y}\right)\right)^T \\ &\cong (\mathbf{cost}_i + \mathbf{Jac}_i \cdot \Delta\mathbf{Y}) \cdot \boldsymbol{\Omega} \cdot (\mathbf{cost}_i + \mathbf{Jac}_i \cdot \Delta\mathbf{Y})^T \\ &= \mathbf{cost}_i \cdot \boldsymbol{\Omega} \cdot \mathbf{cost}_i^T + 2 \cdot \mathbf{cost}_i \cdot \boldsymbol{\Omega} \cdot \mathbf{Jac}_i \cdot \Delta\mathbf{Y} \\ &\quad + \Delta\mathbf{Y}^T \cdot \mathbf{Jac}_i^T \cdot \boldsymbol{\Omega} \cdot \mathbf{Jac}_i \cdot \Delta\mathbf{Y} \\ &= c_i + 2 \cdot \boldsymbol{\Gamma}_i \cdot \Delta\mathbf{Y} + \Delta\mathbf{Y}^T \cdot \boldsymbol{\Lambda}_i \cdot \Delta\mathbf{Y}. \end{aligned} \tag{40}$$

Therefore, the cost function $\mathbf{F}(\mathbf{Y})$ is

$$\begin{aligned}\mathbf{F}\left(\tilde{\mathbf{Y}} + \Delta\mathbf{Y}\right) &= \sum \mathbf{cost}_i \cdot \boldsymbol{\Omega} \cdot (\mathbf{cost}_i)^T \\ &= \sum c_k + \sum 2 \cdot \boldsymbol{\Gamma}_i \cdot \Delta\mathbf{Y} + \sum \Delta\mathbf{Y}^T \cdot \boldsymbol{\Lambda}_i \cdot \Delta\mathbf{Y} \\ &= c + 2 \cdot \boldsymbol{\Gamma} \cdot \Delta\mathbf{Y} + \Delta\mathbf{Y}^T \cdot \boldsymbol{\Lambda} \cdot \Delta\mathbf{Y}. \end{aligned} \tag{41}$$

Second, by taking the derivative of (41) with respect to $\Delta\mathbf{Y}$ and setting the derivative equal to 0, the following equation is obtained:

$$\boldsymbol{\Lambda} \cdot \Delta\mathbf{Y} = -\boldsymbol{\Gamma}. \tag{42}$$

When a damping factor $\boldsymbol{\lambda}$ is added to (42), the new equation is

$$(\boldsymbol{\Lambda} + \lambda \cdot \mathbf{I})\Delta\mathbf{Y} = -\boldsymbol{\Gamma}. \tag{43}$$

An increment $\Delta\mathbf{Y}^*$ is obtained by solving (43); then, the vector is updated as follows:

$$\tilde{\mathbf{Y}} = \tilde{\mathbf{Y}} + \Delta\mathbf{Y}^*. \tag{44}$$

Finally, the first and second steps are repeated until certain conditions are met, e.g., the number of iterations reaches a set value or the increment $\Delta\mathbf{Y}^*$ is less than a predefined threshold. $\tilde{\mathbf{Y}}$ is the final value of the estimated vector. Additionally, the damping factor $\boldsymbol{\lambda}$ affects the iterative process. Selecting a suitable value of this damping factor can contribute to quicker convergence of the estimation process [41], [42].

C. Comparison Between the KF and FGO Methods

The KF method is equivalent to finding the state vector by minimizing the cost functions of the state transformation and the measurements in two consecutive epochs. However, the following drawbacks restrict its performance.

1) Uncertainty in the state vector $\Delta\mathbf{x}_k$ will degrade the estimation through the transformation matrix $\mathbf{F}_{k,k+1}$, and the estimation of the state vector $\Delta\mathbf{x}_k$ is accomplished in the previous epoch. Adding more state vectors to the cost function might contribute to improved estimation of these state vectors.
2) The state transformation matrix $\mathbf{F}_{k,k+1}$ and the observation matrix $\mathbf{H}_{k+1}$ might be nonlinear; hence, the linearization applied by the KF might degrade the state vector estimation.

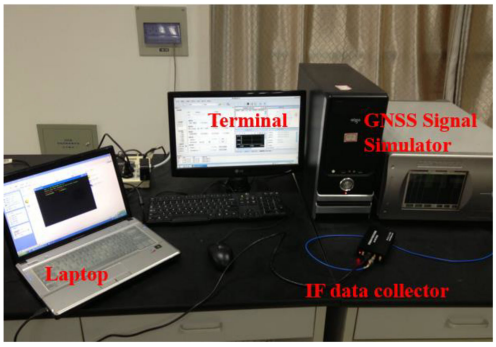

Fig. 3. IF signal collection.

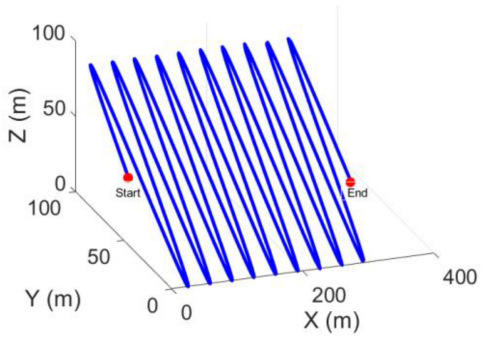

Fig. 4. 3-D trajectory.

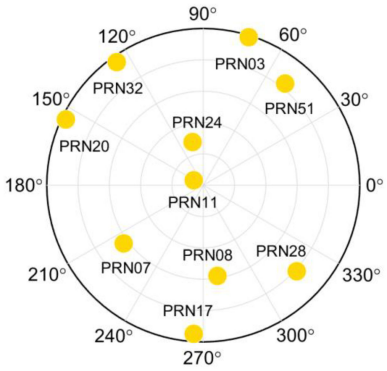

Fig. 5. Satellite distribution [8].

3) When the signal conditions change from LOS to NLOS, the state and measurement models also change. In the KF method, the corresponding matrices, e.g., the state estimation error covariance matrix, the KF gain matrix, and the state transformation matrix, need to be reconstructed.

FGO is a method of finding the optimal estimate of the state vectors minimizing all error functions. A set of state vectors is estimated simultaneously by minimizing the total error function. In this manner, superior estimation of the state vectors is expected compared with the KF method. In each epoch, all or part of the past state vectors are estimated again. These cost functions can be regarded as constraints on these state vectors in FGO. The relationship between these state vectors and error functions is presented in Fig. 2. Compared with the KF method, the characteristics of the FGO method can be summarized as follows.

1) The FGO method optimizes all states together in each epoch. Compared with the KF method, FGO can alleviate the detrimental effect of the uncertainty of the previous state vector, and the historical information employed in the estimation process can contribute to smoother results compared with the KF results.
2) FGO can work in a plug-and-play manner. For example, the measurements might change due to the available satellites in view; in the KF method, the corresponding matrices must be reconstructed when the measurement vectors or the state vectors change, whereas the state vector in our proposed method is simply augmented with the NLOS-induced bias when the signal conditions change from LOS to NLOS.
3) The VT measurement model is nonlinear, and Section III presents the linearized model. As presented in Section III-B, a linearization operation is repeated in the LM method to iteratively find the optimal estimate of the state vectors. Thus, FGO can contribute to superior performance compared with the linear KF method.

V. Experiments and Results

With the aim of fully assessing the performance of the proposed method, a simulation test and two field tests were carried out. A GPS L1 data set was collected and selected as an example in the experiments. In the first simulation test, we employed a GNSS signal simulator to generate a signal with a given input trajectory. A GNSS IF collector was connected to a laptop and utilized to sample and convert the GNSS signal (Fig. 3). Then, the developed VT software was used to process the collected IF data set and obtain the navigation solutions.

In the second and third experiments, we collected data sets in a real environment. Both static and dynamic GPS L1 data sets were collected; specifically, in the dynamic GPS L1 data set, LOS/NLOS signal reception changes occurred along with the motion.

A. Dynamic Simulation Test

The dynamic trajectory used in the simulation is presented in Fig. 4. The time length was approximately 330 s. The satellite distribution is presented in Fig. 5; note that we generated the GNSS signals using the same ephemeris settings as in our previous paper [8]. We utilized both the KF-VT and FGO-VT methods to process the IF data set, and the horizontal positioning errors are presented in Fig. 6. It can be observed that FGO-VT exhibited superior performance, and the statistical analysis results are listed in Table I. Specifically, the mean values of the horizontal positioning errors from FGO-VT are lower by 36.4% compared with KF-VT, and the mean square errors (MSEs) are lower by 29.2%. Note that here, we utilized the GNSS signal simulator to generate "clean" signals.

With the aim of assessing the performance of FGO-VT under NLOS conditions, we then added a bias to the code discriminator outputs; specifically, we added a simulated

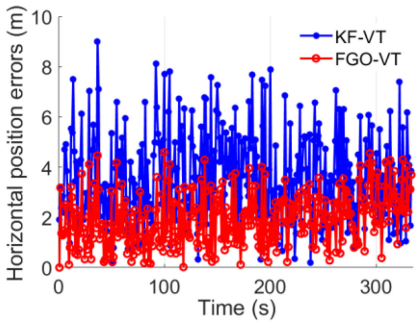

Fig. 6. Horizontal positioning errors.

TABLE I
STATISTICAL ANALYSIS OF THE HORIZONTAL POSITIONING ERRORS

Method	Mean (m)	MSE (m)
KF-VT	3.05	1.54
FGO-VT	1.94	1.05

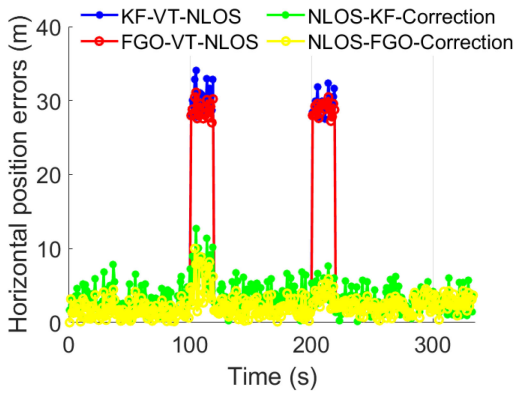

Fig. 7. Horizontal positioning errors.

NLOS-induced bias of 50 m to PRN 08 during 100–120 s and 200–220 s. Fig. 7 presents the horizontal positioning error comparison, from which the following can be observed.

1) KF-VT and FGO-VT are both affected by NLOS-induced bias, with most horizontal positioning errors being larger than 25 m.
2) KF-VT-Correction and FGO-VT-Correction are both effective for mitigating NLOS-induced errors, although the horizontal positioning errors are still larger than those under normal conditions. Table II lists the horizontal positioning errors from KF-VT-Correction and FGO-VT-Correction under NLOS conditions, from which it can be seen that FGO-VT-Correction achieves superior performance.

B. Static Field Testing

In addition to the simulation, we carried out a field test to assess the performance of the proposed method. Table III presents the parameters and details of the GPS L1 collector (NSL Stereo) and the employed antenna (right-handed circularly polarized). The sampling frequency was 26 MHz, and the intermediate frequency (IF) was 0 MHz.

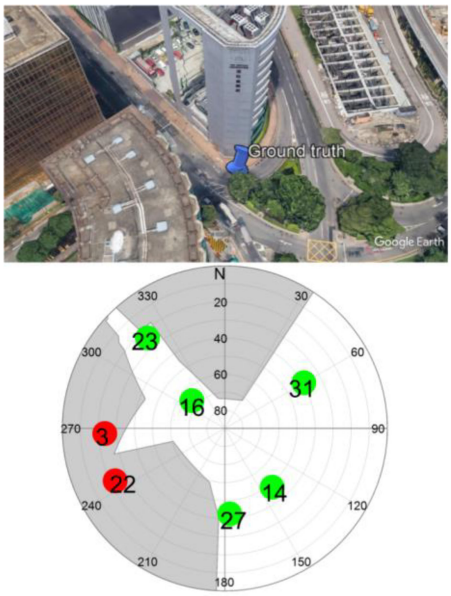

Fig. 8. GPS L1 IF signal data set collection site on Google Earth and the corresponding sky visibility plot [45].

TABLE II
STATISTICAL ANALYSIS OF THE HORIZONTAL POSITIONING ERRORS

Method	Mean (m)		MSE (m)	
	100~120	200~220	100~120	200~220
KF-VT -Correction	7.34	4.48	2.75	1.62
FGO-VT -Correction	5.26	2.75	2.65	1.20

TABLE III
PARAMETER SETTINGS OF DATA COLLECTION EQUIPMENT [15], [38], [45]

Equipment	Parameter	Value	Unit
Antenna	Model	AGR6303	-
	Polarization	Right-handed circularly polarized	-
Front-end	Model	NSL Stereo	-
	GNSS signal	GPS L1 C/A	-
	Sampling frequency	26	MHz
	Intermediate frequency	0	MHz
	Gain	10	dB

A crossroad in Hong Kong was selected as the data set collection site. Fig. 8(a) presents the data set collection site plotted on Google Earth. Satellite visibility is plotted in Fig. 8(b) with the building boundary information extracted from the 3-D map. As presented, seven satellites were acquired and well tracked in this test data set with the GPS L1 signal. Among them, the PRN 3 and 22 signal sources were NLOS satellites. The surrounding tall buildings blocked direct signals from PRN 3 and PRN 22. The surfaces of the buildings reflected the tracked signals. The signal strength is presented in Fig. 9, and it can be observed that the PRN 3 and 22 signal strengths were lower than those of the remaining satellites. The signal

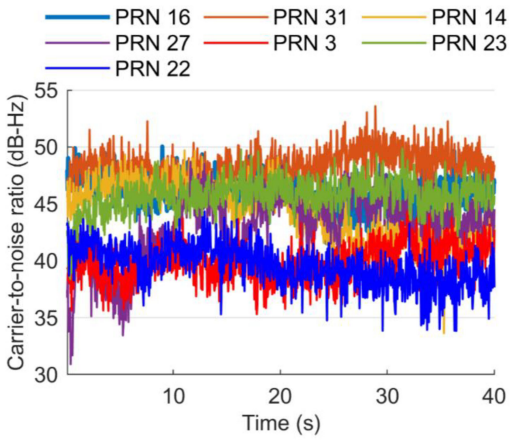

Fig. 9. Signal strength [45].

strength loss was induced by signal reflection. Note that this data set was also utilized in our previous paper [45], some results were different since the VT parameters were different.

Fig. 10 presents the latitude, longitude, and horizontal positioning errors, and the cumulative distribution function (CDF) of the horizontal positioning errors is presented in Fig. 6. The legend "KF-VT-NLOS" indicates the Kalman-filter-based VT method without any means of addressing NLOS reception. The legend "KF-VT-Exclusion" refers to KF-VT with NLOS-contaminated measurements excluded. Here, PRN 3 and PRN 22 were excluded while employing the other measurements for VT to estimate the navigation solutions. The legend "KF-VT-Correction" indicates the use of multiple correlators for correction based on NLOS reception detection. The NLOS-induced errors were extracted from multiple correlators. As seen from the correlator outputs for LOS and NLOS signals presented in Fig. 1, NLOS reception induces a code phase bias between the peak in the correlator output and the prompt correlator output with a code phase of zero. The legend "FGO-VT-Correction" indicates the FGO-VT method with multicorrelator-based NLOS correction. In the FGO-VT-Correction method, the NLOS-induced code phase bias was added to the state vector of the navigation filter, and the code phase bias extracted from the multiple correlators was set as the initial value of the state vector. Then, the iterative method presented in Section III-B was employed to optimize the state vector estimation.

By comparing the positioning errors from the four methods, the following can be observed.

1) Either not addressing NLOS reception or directly excluding NLOS-contaminated measurements greatly exacerbates the positioning error. The green lines in Fig. 10 represent the positioning errors of the KF-VT-Exclusion method, in which PRN 3 and PRN 22 were excluded; as a result, the in-view satellite geometry distribution worsened, and the positioning error increased. The red lines represent the positioning errors of the KF-VT-NLOS method, in which the inclusion of NLOS-influenced measurements in the navigation solution estimation process degraded the positioning accuracy.
2) The blue and yellow lines represent the positioning errors of the KF-VT-Correction and FGO-VT-Correction methods. Compared with the KF-VT-NLOS and KF-VT-Exclusion methods, the positioning errors showed a noticeable decrease after NLOS-induced code phase bias correction; the results of a statistical analysis of these positioning errors are listed in Table IV. After correction, the mean and MSE were smaller than 8 and 4 m, respectively.

Furthermore, we observe that FGO-VT-Correction achieved superior performance compared to the KF-VT-Correction method. When the KF was substituted with FGO, the mean

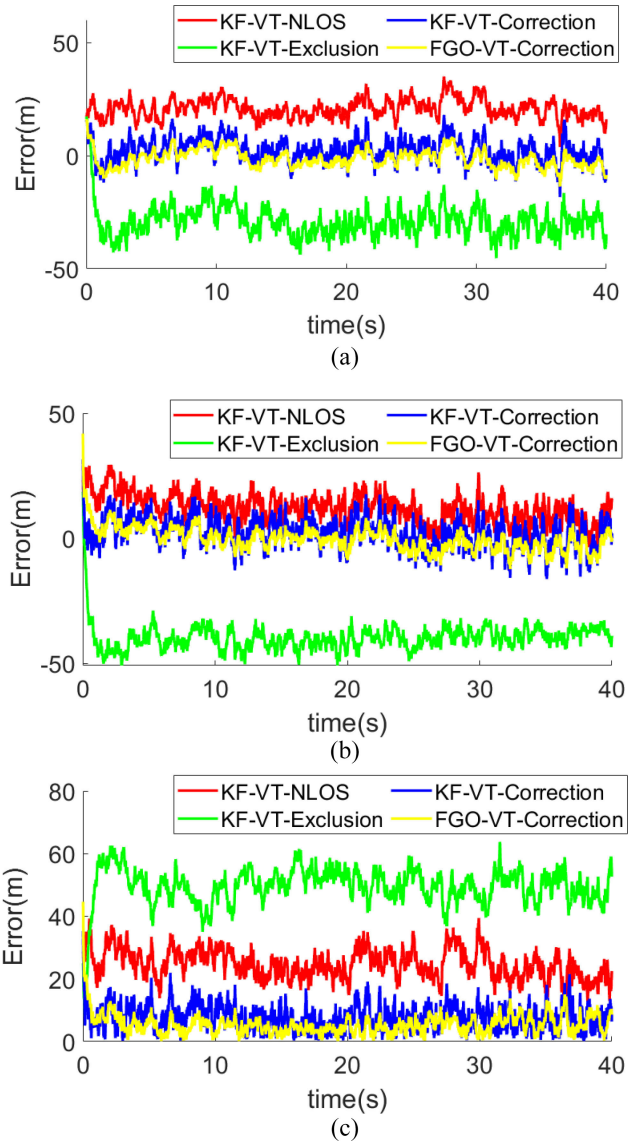

Fig. 10. Positioning errors. (a) Latitude errors. (b) Longitude errors. (c) Horizontal positioning errors.

TABLE IV
STATISTICAL ANALYSIS OF THE HORIZONTAL POSITIONING ERRORS

Method	Mean (m)	MSE (m)
KF-VT-NLOS	24.8	4.6
KF-VT-Exclusion	49.6	5.9
KF-VT-Correction	7.6	3.8
FGO-VT-Correction	5.4	3.1

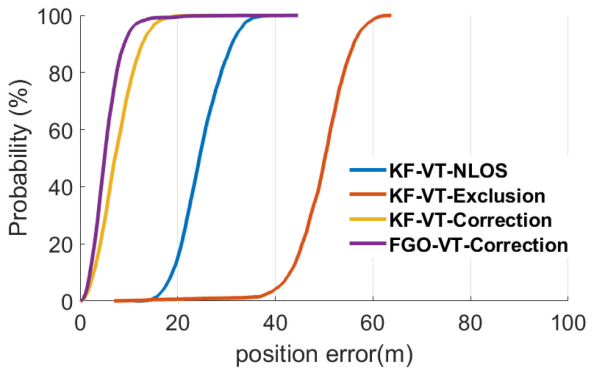

Fig. 11. CDF of the horizontal positioning errors.

and standard deviation values decreased by 28.9% and 18.4%, respectively. Additionally, improvements can be observed from the CDF of the positioning errors plotted in Fig. 11. We suggest that the following factors likely contributed to these improvements.

1) In FGO, state vectors from past and current epochs are optimized together in an iterative process, and smoother results are obtained. Here, only ten state vectors were optimized together in the current epoch because of computational load considerations.
2) The NLOS-induced bias is added to the state vector; thus, its estimation was also optimized, which might contribute to the superior performance of the KF-VT-Correction method.

C. Dynamic Field Testing With Real NLOS Conditions

In addition to the static field test, a GPS L1 IF data set collected with a dynamic trajectory was employed to assess the proposed method (this dynamic IF GPS L1 data set was the same as that used in our previous paper [15], [45]). Fig. 12 presents street views of the data set collection site, the data set collection trajectory, and the in-view satellite distributions. In the experiment, the antenna was carried by a pedestrian walking from Point #1 to Point #2 and then back to Point #1. Specifically, the details of the trajectory were as follows.

1) The pedestrian first stood unmoving at Point #1 for 40 s. The corresponding in-view satellite distribution is plotted in Fig. 12 (bottom left panel of the figure), containing five "healthy" satellites (PRN 14, PRN 22, PRN 26, PRN 31, and PRN 32).
2) Then, the pedestrian walked to Point #2 and stopped for several seconds. Similarly, the satellite distribution at Point #2 is plotted in the bottom right panel of Fig. 12. In this case, PRN 31 produce an NLOS signal because the elevation angle of PRN 31 was lower than the building boundary.
3) Finally, the pedestrian walked back to Point #1 along the same route. Fig. 13 presents the eastward velocity, which is consistent with the above description of the route.

Fig. 14 presents the horizontal positioning errors of the KF-VT-Correction and FGO-VT-Correction methods and the corresponding CDF results for these positioning errors. It

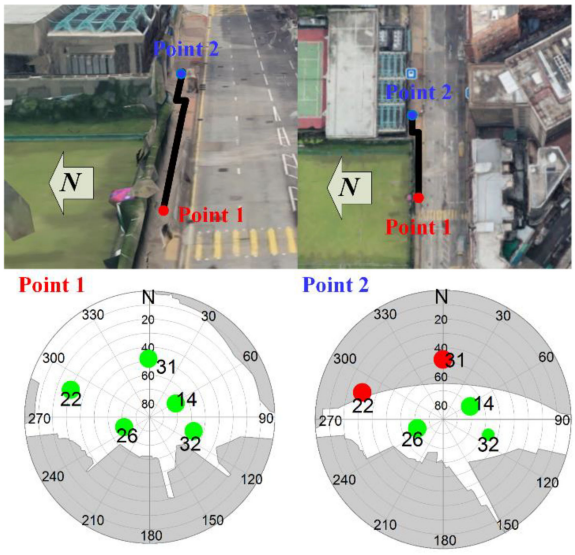

Fig. 12. Street views and the satellite distributions at the two marked points [45].

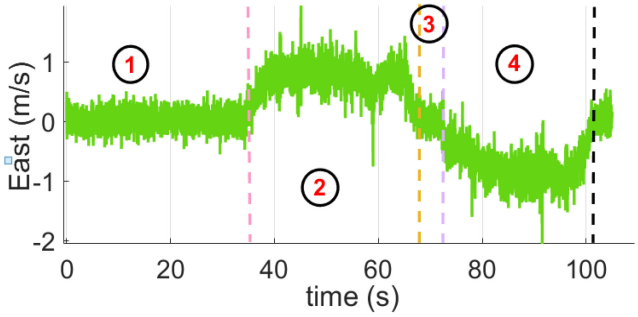

Fig. 13. Eastward velocity [45].

can be observed that the FGO-VT-Correction method outperformed the KF-VT-Correction method, similar to the static test. Fig. 14(b) presents the CDF results for these positioning errors, which show that the positioning error distribution was also improved. Specifically, the FGO-VT-Correction positioning errors were distributed in a narrow range, and the maximum value of the positioning error was also decreased.

D. Discussion

In this article, the NLOS-induced bias was added to the state vector and optimally estimated with an FGO method. Superior performance was obtained by substituting this FGO method for the KF method in the VT technique. However, we can identify the following limitations and restrictions of this work.

1) In this study, the VT program was implemented in MATLAB 2018B, and the implementations of the multiple correlators and the FGO method were computation intensive. It would be of great significance to investigate how to reduce the computational load. Fig. 15 presents the average run time of FGO-VT for 100 iterations of the first experiment. Because of the heavy computational load, we ran for four seconds 100 times, and it took several hours to process the entire data set. As presented in Fig. 15, FGO takes

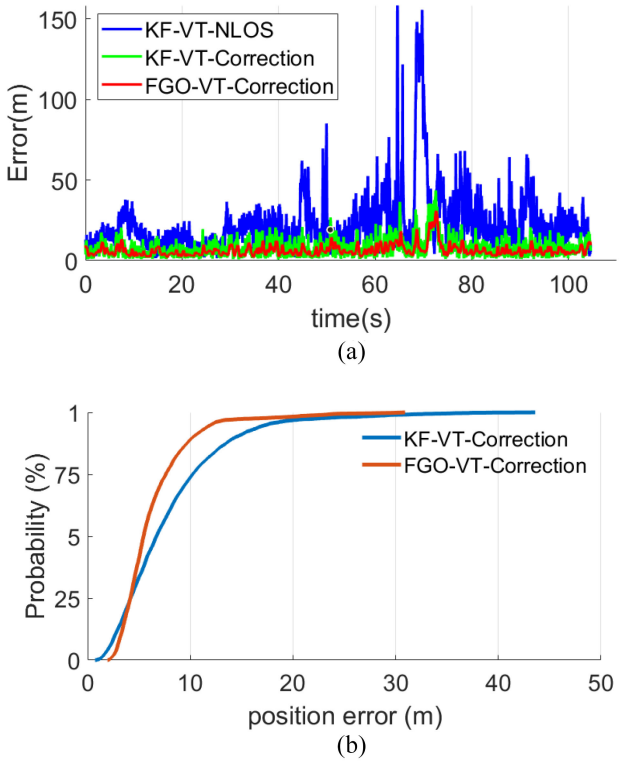

Fig. 14. Positioning errors and CDF. (a) Horizontal positioning errors. (b) CDF of the horizontal positioning errors.

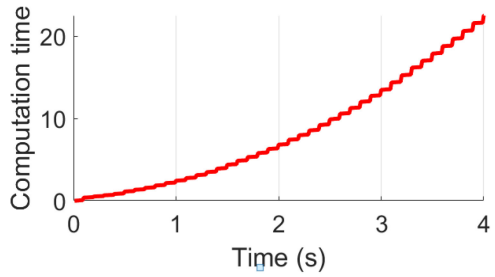

Fig. 15. Computation time for FGO-VT.

approximately 20 s, whereas the KF method takes only approximately 3 s. Note that the computation time refers only to the KF or FGO computation; the multiple correlators are not included. The update frequency of the VT navigation filter is 1000 Hz to maintain signal tracking.

2) NLOS signals are attenuated due to reflection. As a result, the statistical parameters of the noise change; therefore, adaptive measurement matrix tuning might contribute to better estimation of the navigation solutions. In fact, the process and measurement noise components did not strictly follow Gaussian distributions. It would be meaningful to investigate methods for addressing this problem to improve the estimation accuracy.

VI. Conclusion

In this article, we proposed an FGO-based VT method for NLOS-induced bias estimation and correction. The NLOS-induced bias was added to the state vector, which was optimally estimated using the FGO method. Three different GPS L1 IF data sets were employed to assess the proposed method. Based on the experimental results, the following conclusions were drawn.

1) NLOS correction effectively reduces the positioning error; correction is better than mitigation or exclusion.
2) FGO-VT outperforms KF-VT. Additionally, FGO-VT can decrease the positioning errors under NLOS conditions.
3) The VT measurement model is usually nonlinear. In conventional KF-VT, the measurement model is first linearized. The iterative process in FGO might effectively alleviate the detrimental effect of the nonlinear model on navigation solution estimation.

References

[1] Y. Li *et al.*, "Toward location-enabled IoT (LE-IoT): IoT positioning techniques, error sources, and error mitigation," *IEEE Internet Things J.*, vol. 8, no. 3, pp. 4035–4062, Mar. 2021, doi: 10.1109/JIOT.2020.3019199.

[2] A. Vashist *et al.*, "Indoor wireless localization using consumer-grade 60 GHz equipment with machine learning for intelligent material handling," in *Proc. IEEE Int. Conf. Consum. Electron. (ICCE)*, 2020, pp. 1–6.

[3] Y. Li, Z. He, Z. Gao, Y. Zhuang, C. Shi, and N. El-Sheimy, "Toward robust crowdsourcing-based localization: A fingerprinting accuracy indicator enhanced wireless/magnetic/inertial integration approach," *IEEE Internet Things J.*, vol. 6, no. 2, pp. 3585–3600, Apr. 2019, doi: 10.1109/JIOT.2018.2889303.

[4] Y. Xu, Y. S. Shmaliy, C. K. Ahn, T. Shen, and Y. Zhuang, "Tightly coupled integration of INS and UWB using fixed-lag extended UFIR smoothing for quadrotor localization," *IEEE Internet Things J.*, vol. 8, no. 3, pp. 1716–1727, Feb. 2021, doi: 10.1109/JIOT.2020.3015351.

[5] Y. Zhuang, Q. Wang, M. Shi, P. Cao, L. Qi, and J. Yang, "Low-power centimeter-level localization for indoor mobile robots based on ensemble Kalman smoother using received signal strength," *IEEE Internet Things J.*, vol. 6, no. 4, pp. 6513–6522, Aug. 2019, doi: 10.1109/JIOT.2019.2907707.

[6] C. Jiang, S. Chen, Y. Chen, J. Shen, D. Liu, and Y. Bo, "Superior position estimation based on optimization in GNSS," *IEEE Commun. Lett.*, vol. 25, no. 2, pp. 479–483, Feb. 2021, doi: 10.1109/LCOMM.2020.3024791.

[7] P. D. Groves, "Principles of GNSS, inertial, and multisensor integrated navigation systems," *IEEE Trans. Aerosp. Electron. Syst. Mag.*, vol. 30, no. 2, pp. 26–27, Feb. 2015.

[8] C. Jiang, S. Chen, Y. Chen, and Y. Bo, "Research on a chip scale atomic clock aided vector tracking loop," *IET Radar Sonar Navigat.*, vol. 13, no. 7, pp. 1101–1106, 2019.

[9] P. D. Groves and Z. Jiang, "Height aiding, C/N_0 weighting and consistency checking for GNSS NLOS and multipath mitigation in urban areas," *J. Navigat.*, vol. 66, no. 5, pp. 653–669, 2013.

[10] A. Bourdeau, M. Sahmoudi, and J.-Y. Tourneret, "Constructive use of GNSS NLOS-multipath: Augmenting the navigation Kalman filter with a 3D model of the environment," in *Proc. 15th Int. Conf. Inf. Fusion*, 2012, pp. 2271–2276.

[11] P. D. Groves, Z. Jiang, L. Wang, and M. K. Ziebart, "Intelligent urban positioning using multi-constellation GNSS with 3D mapping and NLOS signal detection," *Proc. ION GNSS*, Sep. 2012, pp. 458–472.

[12] T. Suzuki, Y. Nakano, and Y. Amano, "NLOS multipath detection by using machine learning in urban environments," in *Proc. 30th Int. Tech. Meeting Satellite Div. Inst. Navigat. (ION GNSS+)*, 2017, (pp. 3958–3967).

[13] H. Xu, A. Angrisano, S. Gaglione, and L. T. Hsu, "Machine learning based LOS/NLOS classifier and robust estimator for GNSS shadow matching," *Satellite Navigat.*, vol. 1, no. 1, pp. 1–12, 2020.

[14] Z. Lyu and Y. Gao, "A new method for non-line-of-sight GNSS signal detection for positioning accuracy improvement in Urban environments," in *Proc. 33rd Int. Tech. Meeting Satellite Div. Inst. Navigat. (ION GNSS+)*, 2020, pp. 2972–2988.

[15] B. Xu, Q. Jia, Y. Luo, and L. T. Hsu, "Intelligent GPS L1 LOS/multipath/NLOS classifiers based on correlator-, RINEX-and NMEA-level measurements," *Remote Sens.*, vol. 11, no. 16, p. 1851, 2019.
[16] R. Sun, G. Wang, W. Zhang, L. T. Hsu, and W. Y. Ochieng, "A gradient boosting decision tree based GPS signal reception classification algorithm," *Appl. Soft Comput.*, vol. 86, Jan. 2020, Art. no. 105942.
[17] Q. Liu, Z. Huang, and J. Wang, "Indoor non-line-of-sight and multipath detection using deep learning approach," *GPS Solut.*, vol. 23, no. 3, p. 75, 2019.
[18] C. Jiang, J. Shen, S. Chen, Y. Chen, D. Liu, and Y. Bo, "UWB NLOS/LOS classification using deep learning method," *IEEE Commun. Lett.*, vol. 24, no. 10, pp. 2226–2230, Oct. 2020.
[19] S. Tongleamnak and M. Nagai, "Simulation of GNSS availability in Urban environments using a panoramic image dataset," *Int. J. Navigat. Observ.*, vol. 2017, Jan. 2017, Art. no. 8047158.
[20] J. Moreau, S. Ambellouis, and Y. Ruichek, "Fisheye-based method for GPS localization improvement in unknown semi-obstructed areas," *Sensors*, vol. 17, no. 1, p. 119, 2017.
[21] T. Suzuki and N. Kubo, "Correcting GNSS multipath errors using a 3D surface model and particle filter," in *Proc. 26th Int. Tech. Meeting Satellite Div. Inst. Navigat. (ION GNSS+)*, 2013, pp. 1583–1595.
[22] H. F. Ng, G. Zhang, and L. T. Hsu, "A computation effective range-based 3D mapping aided GNSS with NLOS correction method," *J. Navigat.*, vol. 73, no. 6, pp. 1–21, 2020.
[23] L. Wang, P. D. Groves, and M. K. Ziebart, "Urban positioning on a smartphone: Real-time shadow matching using GNSS and 3D city models," in *Proc. Inst. Navigat.*, 2013, pp. 1606–1619.
[24] J. H. Won, D. Dötterböck, and B. Eissfeller, "Performance comparison of different forms of Kalman filter approach for a vector-based GNSS signal tracking loop," in *Proc. 22nd Int. Tech. Meeting Satellite Div. Inst. Navigat. (ION GNSS)*, 2009, pp. 3037–3048.
[25] S. Zhao and D. Akos, "An open-source GPS/GNSS vector tracking loop-implementation, filter tuning, and results," in *Proc. Int. Tech. Meeting Inst. Navigat.*, 2011, pp. 1293–1305.
[26] Y. Ng and G. X. Gao, "GNSS multireceiver vector tracking," *IEEE Trans. Aerosp. Electron. Syst.*, vol. 53, no. 5, pp. 2583–2593, Oct. 2017.
[27] T. Pany and B. Eissfeller, "Use of a vector delay lock loop receiver for GNSS signal power analysis in bad signal conditions," in *Proc. IEEE/ION Position Location Navigat. Symp.*, 2006, pp. 893–903.
[28] E. M. Copps, G. J. Geier, W. C. Fidler, and P. A. Grundy, "Optimal processing of GPS signals," *Navigation*, vol. 27, no. 3, pp. 171–182, 1980.
[29] J. J. Spilker Jr., "Fundamentals of signal tracking theory," in *Global Positioning System: Theory and Applications*, B. Parkinson, J. J. Spilker Jr., P. Axelrad, and P. Enge, Eds., vol. I. Cambridge, MA, USA: Charles Stark Draper Lab., 1996, pp. 245–327.
[30] M. Lashley, D. M. Bevly, and J. Y. Hung, "Performance analysis of vector tracking algorithms for weak GPS signals in high dynamics," *IEEE J. Sel. Topics Signal Process.*, vol. 3, no. 4, pp. 661–673, Aug. 2009.
[31] E. Amani *et al.*, "Adaptive and conjoint scalar-vector tracking loops for GNSS tracking robustness and positioning integrity," in *Proc. Eur. Navigat. Conf. (ENC)*, 2017, pp. 1–13.
[32] S. Bhattacharyya and D. Gebre-Egziabher, "Integrity monitoring with vector GNSS receivers," *IEEE Trans. Aerosp. Electron. Syst.*, vol. 50, no. 4, pp. 2779–2793, Oct. 2014.
[33] T. Lin, C. O'Driscoll, and G. Lachapelle, "Development of a context-aware vector-based high-sensitivity GNSS software receiver," in *Proc. Int. Tech. Meeting Inst. Navigat.*, 2011, pp. 1043–1055.
[34] F. Xie, R. Sun, G. Kang, W. Qian, J. Zhao, and L. Zhang, "A jamming tolerant BeiDou combined B1/B2 vector tracking algorithm for ultra-tightly coupled GNSS/INS systems," *Aerosp. Sci. Technol.*, vol. 70, pp. 265–276, Aug. 2017.
[35] J. Liu, X. Cui, M. Lu, and Z. Feng, "Vector tracking loops in GNSS receivers for dynamic weak signals," *J. Syst. Eng. Electron.*, vol. 24, no. 3, pp. 349–364, 2013.
[36] A. Jafarnia-Jahromi, T. Lin, A. Broumandan, J. Nielsen, and G. Lachapelle, "Detection and mitigation of spoofing attacks on a vector-based tracking GPS receiver," in *Proc. ION ITM*, 2012, pp. 790–800.
[37] D. Liu, Q. Xia, C. Jiang, C. Wang, and Y. Bo, "A LSTM-RNN-assisted vector tracking loop for signal outage bridging," *Int. J. Aerosp. Eng.*, vol. 2020, Art. no. 2975489, Aug. 2020.
[38] B. Xu, Q. Jia, and L. T. Hsu, "Vector tracking loop-based GNSS NLOS detection and correction: Algorithm design and performance analysis," *IEEE Trans. Instrum. Meas.*, vol. 69, no. 7, pp. 4604–4619, Jul. 2020.
[39] L. T. Hsu, S. S. Jan, P. D. Groves, and N. Kubo, "Multipath mitigation and NLOS detection using vector tracking in Urban environments," *GPS Solut.*, vol. 19, no. 2, pp. 249–262, 2015.
[40] R. Kümmerle, G. Grisetti, H. Strasdat, K. Konolige, and W. Burgard, "G^2o: A general framework for graph optimization," in *Proc. IEEE Int. Conf. Robot. Autom.*, 2011, pp. 3607–3613.
[41] R. M. Watson and J. N. Gross, "Robust navigation in GNSS degraded environment using graph optimization," in *Proc. 30th Int. Tech. Meeting Satellite Div. Inst. Navigat. (ION GNSS+)*, 2017, pp. 2906–2918.
[42] N. Sünderhauf, M. Obst, G. Wanielik, and P. Protzel, "Multipath mitigation in GNSS-based localization using robust optimization," in *Proc. IEEE Intell. Veh. Symp.*, 2012, pp. 784–789.
[43] C. Jiang, S. Chen, Y. Chen, D. Liu, and Y. Bo, "GNSS vector tracking method using graph optimization," *IEEE Trans. Circuits Syst. II, Exp. Briefs*, vol. 68, no. 4, pp. 1313–1317, Apr. 2021.
[44] F. Dellaert, *Factor Graphs and GTSAM: A Hands-On Introduction*. Atlanta, GA, USA: Georgia Inst. Technol., 2012.
[45] C. Jiang, B. Xu, and L. T. Hsu, "Probabilistic approach to detect and correct GNSS NLOS signals using an augmented state vector in the extended Kalman filter," *GPS Solut.*, vol. 25, no. 2, pp. 1–14, 2021.

Changhui Jiang received the B.S. degree from Soochow University, Suzhou, China, in 2014, and the Ph.D. degree from Nanjing University of Science and Technology, Nanjing, China, in 2019.

He studied as a visiting Ph.D. student with the Finnish Geospatial Research Institute, Masala, Finland, from December 2017 to November 2018 (sponsored by the China Scholarship Council), where he is currently working as a Research Scientist. He has authored or coauthored over 50 published journal and conference papers. His research interests include hyperspectral LiDAR, GNSS signal processing, and multisensor integration.

Yuwei Chen received the B.E. and M.Sc. degrees from the Department of Information Science and Electronics Engineering, Zhejiang University, Hangzhou, China, in 1999 and 2002, respectively, and the Ph.D. degree in circuits and systems from Shanghai Institute of Technical Physics, Chinese Academy of Sciences, Shanghai, China, in 2005.

He attended the development of the echo detecting sensor for the laser range finder of Chang'e, China's first moon exploration satellite, which proved to be a successful mission in 16 months of on-orbit operation, and prototyped China's first airborne pushbroom laser scanner. He is currently working with the Finnish Geospatial Research Institute, Masala, Finland, as a Research Manager leading a research group on remote sensing electronics, which focuses on developing new remote sensing systems. He is also a Guest Professor with the Academy of Opto-Electronics, Chinese Academy of Sciences, Beijing, China. He holds 13 patents and has authored or coauthored more than 180 scientific papers and book chapters. His research interests include LiDAR, hyperspectral LiDAR, radar, and navigation and positioning.

Bing Xu (Member, IEEE) received the B.Eng. and Ph.D. degrees in network engineering and navigation guidance and control from Nanjing University of Science and Technology, Nanjing, China, in 2012 and 2018, respectively.

He is currently a Research Assistant Professor with the Interdisciplinary Division of Aeronautical and Aviation Engineering, The Hong Kong Polytechnic University, Hong Kong. Prior to holding his current position, he was a Postdoctoral Fellow with The Hong Kong Polytechnic University from August 2018 to April 2020. His research focuses on signal processing in software-defined GNSS receivers.

Jianxin Jia received the B.E. degree in electronic information engineering from Henan Normal University, Xinxiang, China, in 2012, and the Ph.D. degree in electronic science and technology from the University of the Chinese Academy of Sciences, Beijing, China, in 2018.

He is currently a Research Scientist with the Finnish Geospatial Research Institute, Masala, Finland. His research interests include remote-sensing imaging system design and hyperspectral image processing and applications.

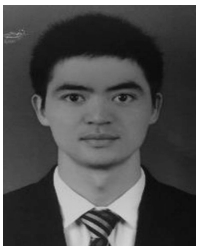

Haibin Sun received the M.E. degree in physics from Harbin Institute of Technology, Harbin, China, in 2012, and the Ph.D. degree in physics from Fudan University, Shanghai, China, in 2016.

He is currently an Assistant Research Fellow with Shanghai Institute of Technical Physics, Chinese Academy of Sciences, Shanghai. His research interests include new optical forming technology and infrared weak target detection technology.

Chen Chen was born in Nantong, China, in 1993. She received the B.E. degree from Nanjing University of Science and Technology, Nanjing, China, where she is currently pursuing the Ph.D. degree in control science and engineering with the School of Automation.

Her research interests include positioning and navigation for autonomous vehicles and personal smartphones in complex urban environments.

Zhiyong Duan was born in Sichuan. He received the B.S. degree in applied physics and the M.E. degree in materials physics and chemistry from Harbin University of Science and Technology, Harbin, China, in 1998 and 2002, respectively, and the Ph.D. degree in microelectronics and solid-state electronics from Shanghai Jiao Tong University, Shanghai, China, in 2005.

He has been a Professor with the School of Physical and Microelectronics, Zhengzhou University, Zhengzhou, China, since 2018. His research interests include nanoimprint lithography, metal interconnects, and MEMS/NEMS technology for fluid transfer pipes.

Yuming Bo was born in Suzhou, China, in 1965. He received the Ph.D. degree from Nanjing University of Science and Technology, Nanjing, China, in 2005.

He is currently a Professor with the School of Automation, Nanjing University of Science and Technology. He has authored or coauthored over 100 journal articles. His research interests include navigation, control theory, and image processing.

Juha Hyyppä received the M.Sc., Dr.Ing., and Dr.Sc. degrees (Hons.) from Helsinki University of Technology, Espoo, Finland, in 1987, 1990, and 1994, respectively.

He is currently a Distinguished Research Professor and the Director of the Centre of Excellence in Laser Scanning Research (Centre grant from the Academy of Finland) and the Department of Remote Sensing and Photogrammetry, Finnish Geospatial Research Institute, Masala, Finland. His research interests include laser scanning systems, their performance and new applications, especially those related to mobile and ubiquitous laser scanning systems, including autonomous driving, as well as point cloud processing.